Chapter-5

Experimental Analysis of Automotive Radiator

This chapter broadly is divided into three sections. First section deals with the detailed design and fabrication of wind tunnel based radiator set up for evaluating the radiator performance. Second section of this chapter presents the radiator performance with water and optimum PG brine as radiator coolants and the third section presents the use of PG brine based hybrid nanofluids for the determination of radiator performances.

5.1 Design and fabrication of Experimental set up

An effort has been made to develop wind tunnel based radiator test setup to achieve the uniform velocity at radiator cross section. The main design criteria are

(i) Open circuit wind-tunnel.

(ii) Good flow quality.

(iii) Test section is square and the maximum test section length possible in the available space.

(iv) Maximum flow speed in the test section of 9 m/s.

(v) Low noise level and low cost.

A schematic of the experimental setup has been designed and fabricated to investigate the heat transfer and pressure drop analysis for radiator with water and PG brine as coolant shown in Fig.5.1. Experimental setup consists of the closed flow lines, one storage tanks, two heaters (Max. 3kW), a centrifugal pump (Max.18lpm), a flow meter (Max.1500 lph), a forced draft fan (Max.1500 rpm) and rectangular fin and flat tubes radiator (model of Maruti 800 car) with the air flow circuit through wind tunnel.

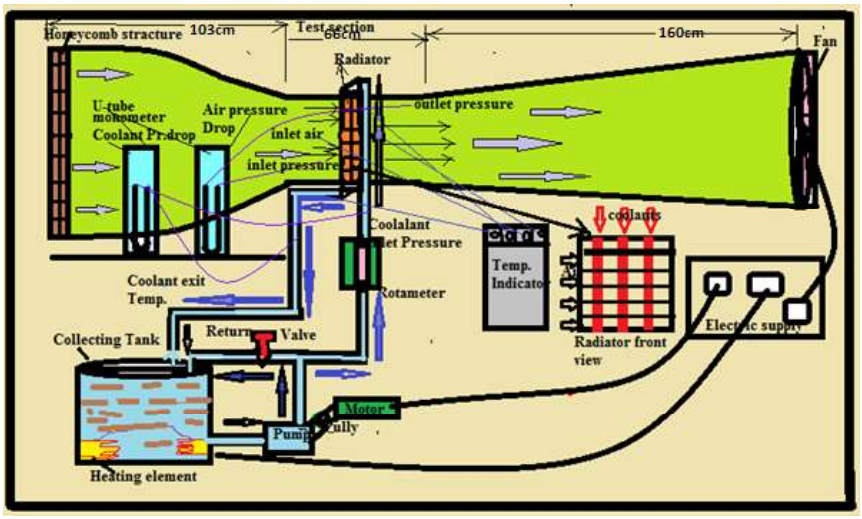

Figure 5.1: Schematic of experimental set up with wind tunnel

Rectangular fin-tube radiator considered here is cross flow type and the core portion consists of vertical flat coolant tubes and rectangular fin, and its dimensions as shown in Fig.5.8. All the dimensions of the radiator has been measured in the laboratory and shown in Table-5.3.

5.2 Description for the several components of wind tunnel based radiator test rig

Test Section: The designed wind tunnel is having a square test chamber with a 0.32 m side and for the desired air velocity of 9 m/s. The test chamber length has to be in the range of (0.5 – 3) * hydraulic diameter [184]. This choice takes into an account that the air flow exiting the nozzle needs 0.5 times the hydraulic diameter to become almost uniform. Moreover, along test chamber (more than 3 times the equivalent hydraulic diameter) could increase boundary layer thickness causing the boundary layer to detach at the test chamber exit. So the length of the test chamber has been taken as 1.8 times the hydraulic diameter of the testing section. The test section length becomes about 66cm as shown in Fig.5.2.

Contraction Cone : The contraction cone area ratio should be as large as possible to reduce the total-pressure loss through the screens mounted between the settling chamber and the cone.

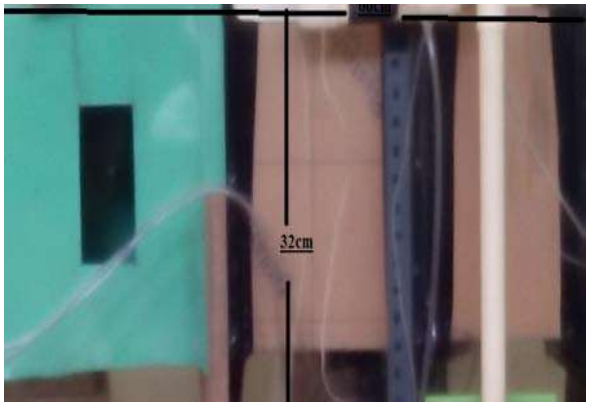

Figure 5.2: Designed test section

Normally, the contraction cone inlet/outlet cross-section area ratio should be in the range 6 - 10 [184]. In this study, an area ratio of 8 has been chosen. The contraction exit length is sensitive to the required length in the test section for a uniform velocity profile. For a contraction ratio of 8, the contraction section length varies from (0.15 – 1) * inlet radius, while the test section settling chamber length should be 1.3 times of the exit radius. Hence, the length of the contraction is found to be 103cm shown in Fig.5.3.

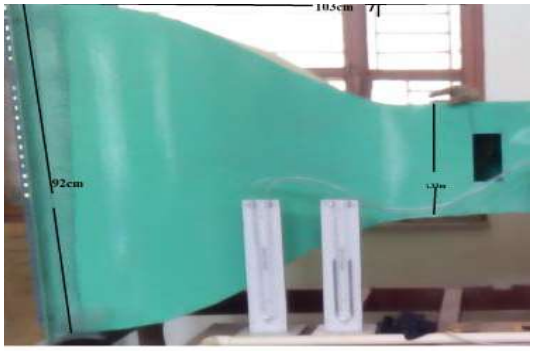

Figure 5.3: Designed contraction cone

Diffuser : The diffuser of a wind tunnel usually extends from downstream end of the test section to the fan. Its main purpose is to reduce velocity in the shortest possible distance to minimize losses. Area ratio of the diffuser should be less than 2.5 and diffuser angle should be $5^{\circ} - 7^{\circ}$ for controlling flow separation. According to these conditions, the diffuser outlet diameter is found to be 60 cm. The minimum length of diffuser can be found from equation given below:

$$\tan \theta = \frac{\sqrt{A_d - 1}}{2L/D_{\mathrm{h}}}$$

Where, D_h is the inlet sections hydraulic diameter andθ is the half of the included angle of the diffuser cone [184]. Solving for L the minimum length of the diffuser is found to be 120 cm. By adjustment of the area ratio, the length of the diffuser is found 160 cm shown in Fig.5.4, which satisfies the above criteria.

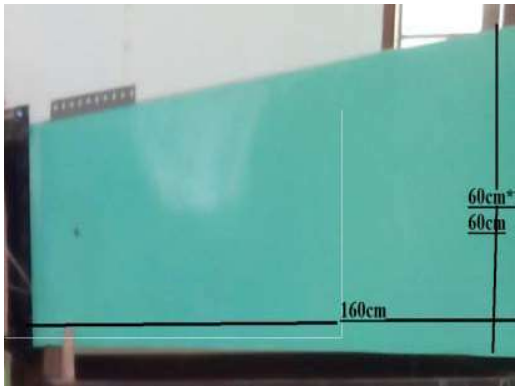

Figure 5.4: Designed diffuser

Settling Chamber : Before the contraction cone there is a settling chamber with a constant cross-sectional area. The aim of a settling chamber which contains honeycombs and screens is to reduce the turbulence flow before it enters the cone. The settling chamber cross-sectional area matches the dimensions of contraction cone inlet diameter. A settling chamber length of 0.5 times the inlet diameter is

often used. Thus, the length of the settling chamber becomes 92cm shown in Fig.5.5.

Figure 5.5: Designed Settling chamber

Honeycomb : A honeycomb with its cells aligned in the flow direction is able to reduce fluctuating variations in transverse velocity as shown in Fig.5.6. The honeycomb has little effect on stream-wise velocity due to the fact that the pressure drop through a honeycomb is small [184]. The primary reason to use a honeycomb is that, it is a very effective flow straightening device. The relatively low pressure drop of a honeycomb makes it rather ineffective in reducing non-uniformities or fluctuations in the stream.

Figure 5.6: Designed honeycomb structure

Wind tunnel set up : The test section of the wind tunnel is constructed according to the design. The test section can be seen from the three sides i.e. front, back and top sides. For making the test section visible, acrylic sheet was used which is

bolted to fix to the test section frame. An opening at the front side is provided to place the anemometer for the measurement of air velocity easily. The leakages have been sealed with M-seal materials. Contraction cone, settling chamber and diffuser have been constructed by 4 mm thick mild steel plate to minimize the construction costs. The most important thing is to fabricate the diffuser section since it has one end rectangular and other end circular due to fan circumference. Specifications and wind tunnel parameters are shown in Table 5.1. Other components and least count of measuring devices are shown in Fig.5.7 and Table 5.2, respectively.

Table: 5.1 Specifications of designed wind tunnel

Wind tunnel parameters	**Value**
Type	Open circuit
Test section length	66cm
Test section cross section	0.32 m × 0.31 m
Mean air velocity range	9 m/s
Overall length	3.29m
Contraction ratio	8
Settling chamber cross section	90cm*90cm
Motor and Fan	2-phase 2kW,

Table 5.2: Least count for all measuring devices

Measuring Device	**Least count**
Rotameter	0.2 lpm
Differential monometer	1 mm
Anemometer	0.1 m/s
Digital temp indicator	$0.1^{o}C$

Figure 5.7: Other components for the radiator experimental setup

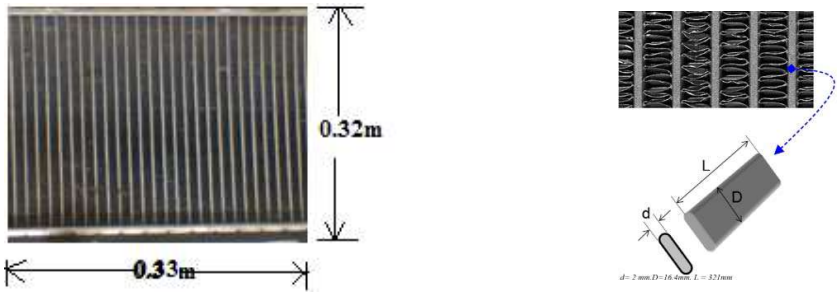

Figure 5.8: Geometric construction of rectangular fin and tube

Table 5.3: Radiator geometry for tubes and fins

Parameters	**Fin side**	**Tube side**
Radiator Width, W_c	321mm	
Radiator height, H_c	334mm	
Core depth, F_d	0.2mm	
Hydraulic diameter	2mm	2.4mm
Tube thickness		0.35mm
Total heat transfer area/total volume	$81.35m^2/m^3$	$3.41m^2/m^3$
Tube dimension		$16.2\times2\times18mm^3$
Number of tubes		33

5.3 Experimental Set up and procedure

The wind tunnel has been designed and fabricated to meet the uniform velocity through the car rectangular radiator made up of aluminium, located at the test section.

After manufacturing of all the components of the wind tunnel and subsequent selection of coolant side components, assembly has been done. A insulated hot water storage tank of total volumetric capacity of 20 litres with temperature controller was used to supply the nanofluids at constant temperature. A magnetic flow meter was used to control and manipulate the flow rate with the precision of 0.2 l/min. K type thermocouples with digital output which has been calibrated by two standard temperature melting point of ice and boiling point of water) were fixed on the flow line to record radiator fluid inlet and outlet temperatures.

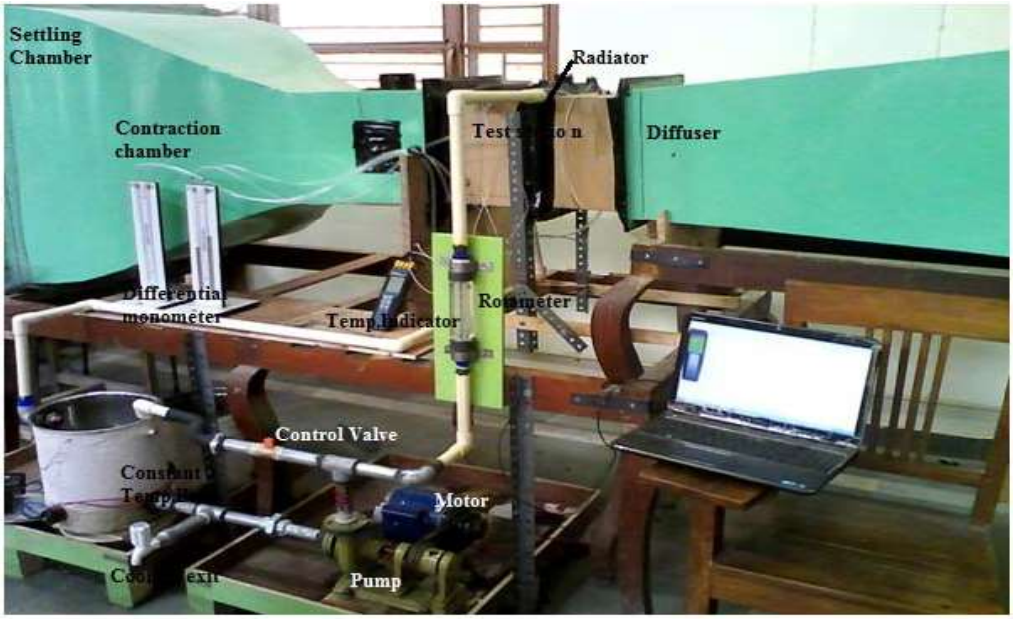

Figure 5.9: Photograph of the fully instrumented radiator experimental setup in wind tunnel

Photograph of fully instrumented experimental setup is shown in Fig. 5.9. Also, other digital thermometers were used for the measurement of air temperature flowing through the wind tunnel. Pressure tapings were made and two manometers were implemented to measure the pressure difference in both air and liquid side circuits. Anemometer was used to measure the air velocity through the tunnel.

5.4 Experimental data Analysis for the radiator performance

The following procedure is followed to obtain heat transfer coefficient of coolant.

Heat transfer rate occurring at coolant side

$$Q_c = m_c * c_{pc} * (T_{ci} - T_{co}) = h_c A(T_b - T_w) \quad (5.1)$$

Where, $m_c = \rho_c * V_c$ (5.2)

$T_b = \frac{T_{ci}+T_{co}}{2}$, T_w is the tube wall temperature which is the mean value of five surface thermocouples.

$$Nu_c = \frac{h_c * Dc}{k_c} \quad (5.3)$$

Coolant-side heat capacity rate is given by:

$$C_c = m_c * c_{pc} \quad (5.4)$$

Coolant pressure drop is given by:

$$\Delta P_c = [G_c^2 * f_f * H_c]/[2 * \rho_f * \left(\frac{D_c}{4}\right)] \quad (5.5)$$

Rate at which heat absorbed by air side,

$$Q_a = m_a * c_{pa} * (T_{ai} - T_{ao}) = h_a A(T_b - T_w) \quad (5.6)$$

Where, $m_a = \rho_a * Ar * u$ (5.7)

$T_b = \frac{T_{ai}+T_{ao}}{2}$, T_w is the fin wall temperature which is the mean value by five surface thermocouples

$$Nu_a = \frac{h_a * Da}{k_a} \quad (5.8)$$

Air-side heat capacity rate is given by:

$$C_a = m_a * c_{pa} \quad (5.9)$$

Heat transfer in radiator,

$$Q = \frac{Q_c + Q_a}{2} \quad (5.10)$$

Cooling effectiveness

$$\varepsilon = \frac{Q_{avg}}{C_{min}\,(C_a, C_c) * (T_{ci} - T_{ai})} \quad (5.11)$$

. For conducting the experimental analysis, all dimensions of rectangular fin radiator have been measured in the laboratories. Thermo-physical and transport properties of both air and coolants have been calculated based on temperature indicator. As the exit temperatures are output parameters and are taken from temperature measuring devices through thermocouples and the inlet temperature of air, coolant and volumetric coolant flow rate are $T_{in,a}$=35^{o}C, $T_{in,f} = 80^oC$ and V_f= 9 l/min respectively.

5.5 Experimental Uncertainties

During experiment with radiator, the temperatures, flow rates, velocity and pressure drops were measured with appropriate instruments. During the measurement of parameters, the uncertainties occurred are presented in Table 5.4. Considering the relative errors in the individual factors as "x_n" ,error estimation of dependent parameter has been made using the following equation [185].

$$W = [\, x_1^2 + x_2^2 + \ldots\ldots\ldots\ldots\ldots + x_n^2 \,]^{1/2} \quad (5.12)$$

The total uncertainties found for estimated results are given in Table 5.5. Repeatability test shows that all sets of experiment data are within the uncertainties limits.

Table 5.4: The uncertainties during the measurements of the experimental parameters

Variable	Uncertainty (%)
Coolant inlet temperature (thermocouple)	± 0.18
Coolant outlet temperature (thermocouple)	±0.18
Air inlet temperature (digital thermometer)	±0.25
Air outlet temperature (digital thermometer)	±0.25
Wall temperature (thermocouple)	±0.18
Coolant mass flow rate	±2.7
Air velocity	±2.1
Coolant side differential pressure	±2.5
Air side differential pressure	±2.4
Coolant thermal conductivity measurement	±5.0
Coolant viscosity measurement	±3.5
Coolant density measurement	±4.0
Coolant specific heat measurement	±5.0

Table 5.5: Total uncertainty results

Reynolds number	5.8%
Heat transfer rate	5.4%
Over all heat transfer coefficient	5.8%
Friction factor	5.9%
Effectiveness	3.4%

5.6. Results and Discussions

5.6.1 Performance comparisons of water and optimum PG brine

As shown in Fig. 5.10, the heat transfer coefficients of water and 25% PG brine are nearly same for experimental and theoretical results within 5.7% deviation. Also, with increase in Reynolds number, the friction factor of optimum PG brine at 70^{o}C - 80^{o}C at a flow rate of 9 l/min, gradually decreases with a experimental and theoretical result of 6.6% deviation as shown in Fig.5.11.

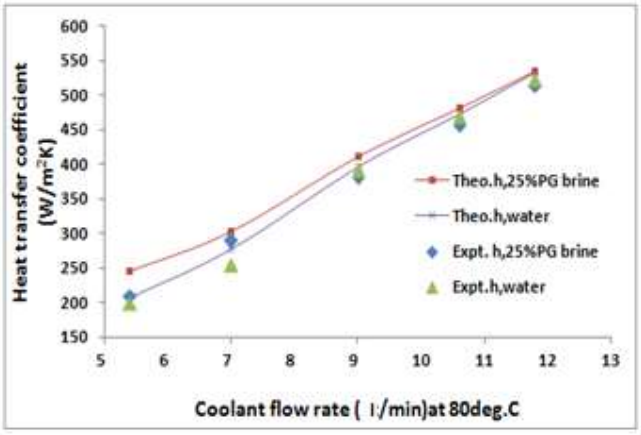

Figure 5.10: Heat transfer coefficient variation (Expt. and Theo.)

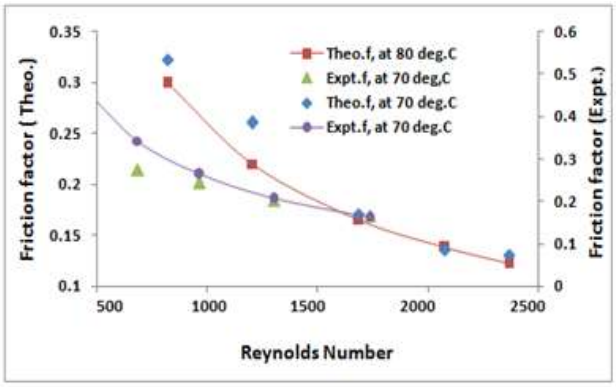

Figure 5.11: Friction factor variation Reynolds number

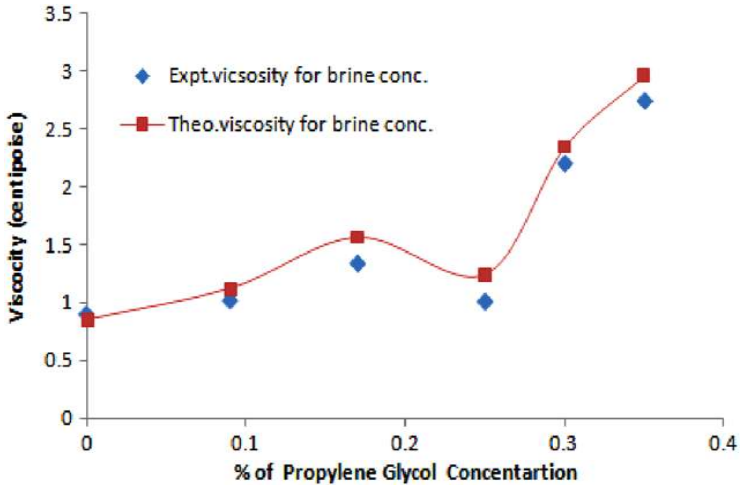

Figure 5.12: Viscosity variation of PG mass fraction

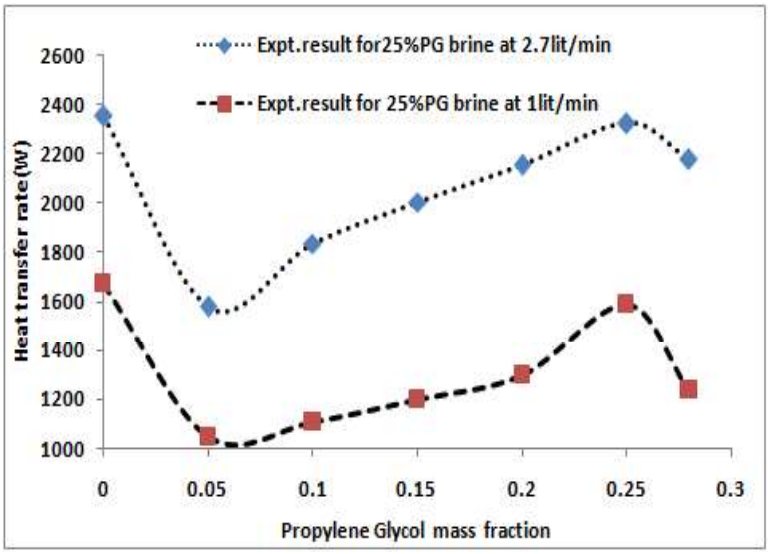

Figure 5.13: Heat transfer rate with PG mass fraction

However, with increase in brine concentration from 0% to 30% (Fig.5.12), the viscosity is minimum at 25% brine concentration with 12% deviation in experimental and theoretical results. As PG is highly soluble in water, and readily metabolized by microbes and higher organisms once released into the environment. The biodegradation process requires oxygen; therefore, dissolved oxygen (DO) concentrations in receiving water may be negatively impacted following a large PG release. With increase in mass fraction of PG brine at inlet temperature of 80^{o}C heat transfer rate initially increases up to 25% concentration and then decreases continuously thereafter; due to low viscosity and it yields nearly the same performance with water at 25% brine solution shown in Fig.5.13.

With this optimum brine concentration (for maximum heat transfer), the viscosity is minimum, which results the increase in Reynolds number due to which, the Nusselt number and heat transfer coefficient increases resulting higher heat transfer rate in rectangular fin radiator as shown in Fig.5.14. Coolant exit temperature for optimum PG brine gradually increases, with increase in coolant

flow rate and yields nearly same performance with water within experimental and theoretical result of 5% deviation as shown in Fig.5.15.

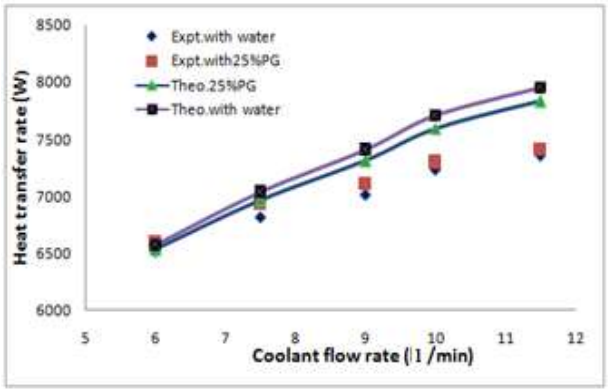

Figure 5.14 : Heat transfer rate variations (Expt. and Theo.)

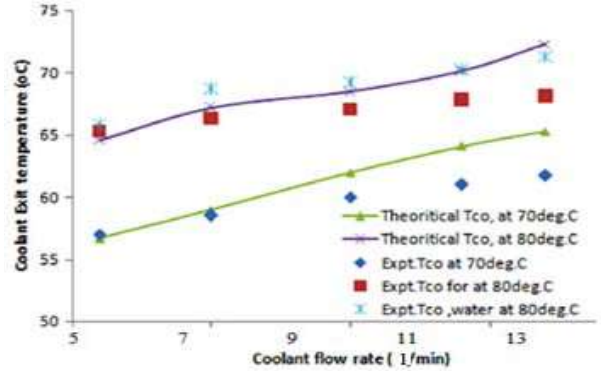

Figure 5.15: Coolant exit temperature (Expt. and Theo.)

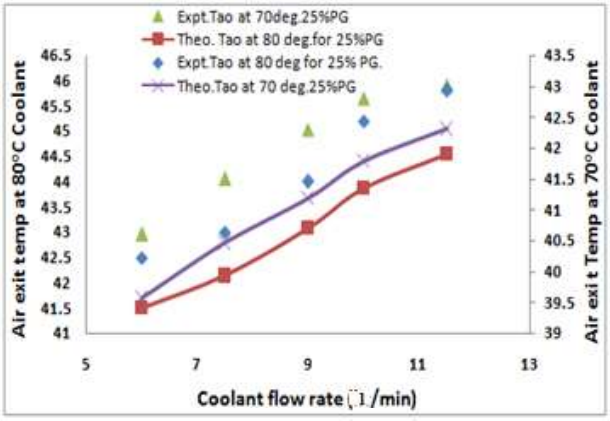

Figure 5.16: Air exit temperature variation (Expt. and Theo.)

Similarly air exit temperature for optimum PG brine gradually increases with both 70°C and 80°C with increase in coolant flow rate and perform nearly same performance as coolant water and the experimental and theoretical result deviation of 3.5% with air frontal velocity of 4.6 m/s in rectangular fin radiator as shown in Fig.5.16.

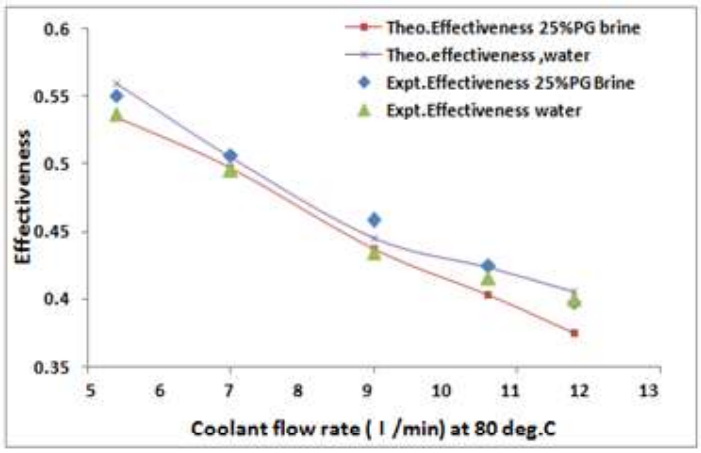

Figure 5.17 : Effectiveness with CFR (Expt. and Theo.)

As shown in Figs. 5.17-5.18, the effectiveness of optimum PG gradually decreases due to increase in the heat capacity rate ratio of both air and coolant side.

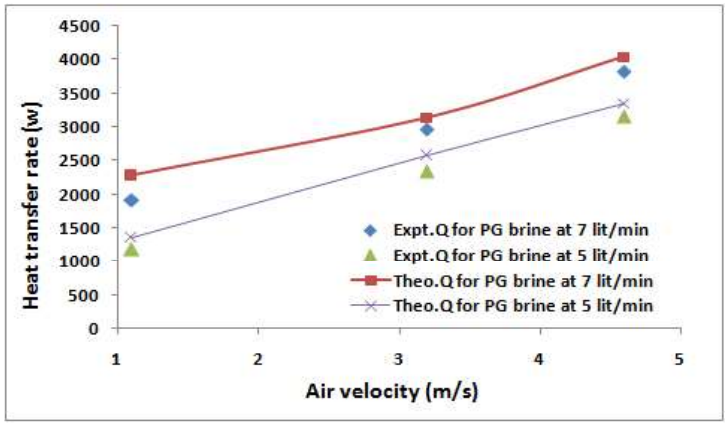

Figure 5.18 : Effectiveness with air velocity (Expt. and Theo.)

The effectiveness of optimum PG brine is nearly same as with water and the3% deviation for both experimental and theoretical result. However, with increase in air frontal velocity, the heat transfer rate gradually increases with experimental and theoretical 6.1% deviation for optimum PG brine at 9 l/min at 80^{o}C as coolant for rectangular fin radiator.

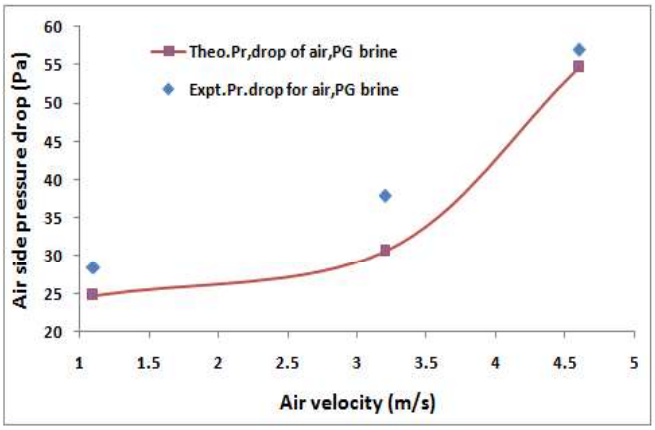

Figure 5.19: Air side pressure drop with air velocity (Expt. and Theo.)

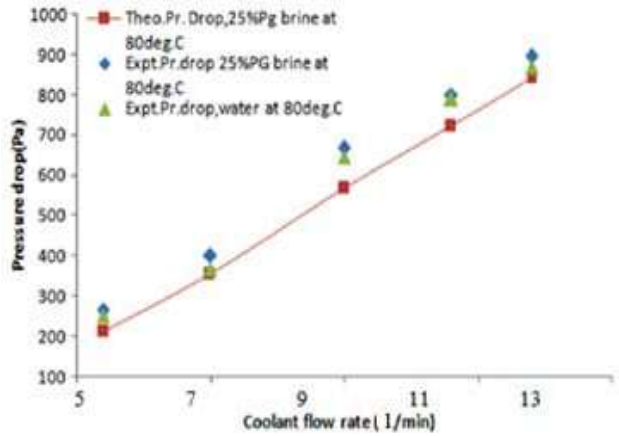

Figure 5.20: Coolant side pressure drop with CFR (Expt. and Theo.)

Air and coolant side pressure drop gradually increases with increase in air velocity and coolant flow rate of optimum PG brine coolant. The increase in

pressure drop is due to the increase in Reynolds number for both air and coolant side. The experimental and theoretical result deviation with 3.66% in air side pressure drop at 4.5m/s, whereas the deviation for coolant pressure drop is 6.6% at 9 l/min and the performance of the pressure drop is nearly same with water (Figs.5.19-5.20) as coolant for automotive radiator.

5.6.2 Hybrid nanofluid preparation

Preparation of hybrid nanofluid is the first key step in the present experimental study. Al_2O_3-PG brine nanofluid is prepared by dispersing 0.5% volume fraction (15 gm) of Al_2O_3 nanoparticles in 8 litre of optimum PG brine(25%PG) using two step method. 1% vol. fraction Span 80 surfactant is added to the solution and then kept under an ultrasonic vibrator (Lark, India), which generating ultrasonic pulses in the power of 180W at 40 kHz. To get a uniform dispersion and stable suspension, which determine the final properties of nanofluids, the nanofluids were kept under ultrasonic vibration continuously for 3h. With this prepared nanofluid 0.5% vol. fraction i.e 16.6 gm of TiO_2 is added for the preparation of 1% volume fraction of hybrid nanofluid, by using ultrasonic vibrator for next 3 hours.

Figure 5.21: Photograph of prepared hybrid nanofluids

With similar procedure 0.5% volume fraction i.e 25.2gm of CuO nano particle is added in prepared PG brine based Al_2O_3 nanofluid, for the preparation

of 1% volume fraction of hybrid nanofluid as coolant for radiator as shown in Fig.5.21 . The key parameters for assessing the heat transfer merits of nanofluids are their thermophysical properties, which have been discussed in Chapter 3.

5.6.3 Performance comparisons of PG brine based hybrid nanofluids

Effects on friction factor, Reynolds number, Nusselt number, effectiveness and coolant pressure drop have been shown in Figs. 5.22-5.23, for a rectangular fin radiator with the application of hybrid nanofluid as radiator coolant. Results show that friction factor of optimum PG brine (25%PG) based Al_2O_3-TiO_2 hybrid nanofluid decreases with increase in Reynolds number. Also, the experimental result of friction factor is deviated by 8% from the theoretical result.

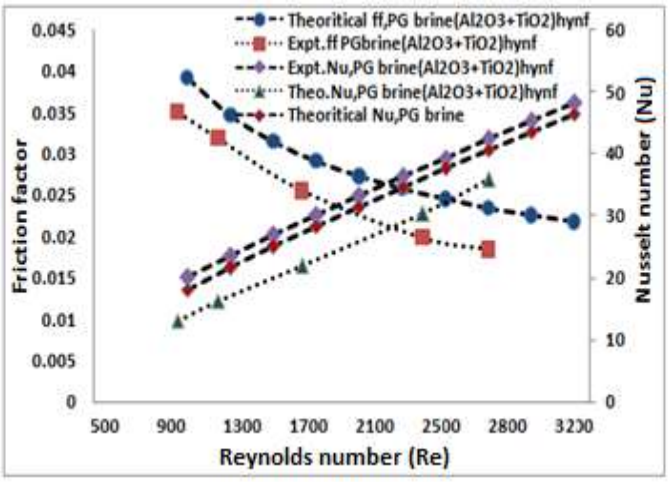

Figure 5.22 : Friction factor and Nusselt number variation

However, Nusselt number of both optimum PG brine (25%PG) based Al_2O_3-TiO_2 hybrid nanofluid and 25%PG brine increases with increase in Reynolds number and the experimental results of Nusselt number is deviated by 9%, 8% from hybrid nanofluid and optimum PG brine, respectively.

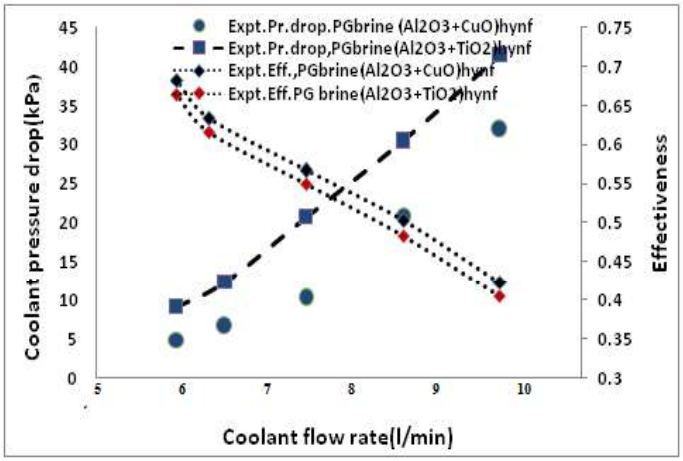

Figure 5.23 : Coolant pressure drop and effectiveness variations

Coolant pressure drop for optimum PG based Al_2O_3-CuO hybrid nanofluid is lower as compared to Al_2O_3-TiO_2 hybrid nanofluid . However, the effectiveness of optimum PG based Al_2O_3-CuO hybrid nanofluid is 5% more as compared to PG based Al_2O_3- TiO_2 hybrid nanofluids and that gradually decreases with increase in coolant flow rate. This is due to increase in the coolant side minimum heat capacity rate.

Variations in heat transfer rate, effectiveness, type of coolant and air exit temperatures with coolant flow rate have been shown in Figs. 5.24-5.25. Results show that the heat transfer rate and effectiveness of optimum PG based Al_2O_3-CuO hybrid nanofluid respectively, are 7.4% and 5.2% higher. This is due to higher heat transfer coefficient as compared to Al_2O_3- TiO_2/PG brine hybrid nanofluid at temperature of 80^oC for a flat tube of rectangular fin radiator. However, coolant exit temperature of Al_2O_3-CuO/PG brine hybrid nanofluid is 8% lower than Al_2O_3-TiO_2/PG brine hybrid nanofluid due to more heat gained by the air side at a frontal velocity of 4.5m/s for rectangular fin radiator.

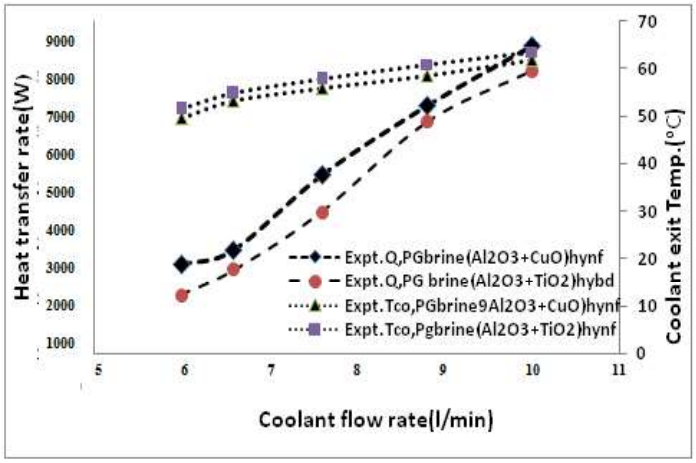

Figure 5.24 : Heat transfer rate and coolant exit temperature

Also, results show that the air exit temperature for Al_2O_3-CuO/PG brine hybrid nanofluid is 9 % higher than PG brine based Al_2O_3- TiO_2 hybrid nanofluid as radiator coolant at a frontal air velocity 4.5m/s. Experimental results for NTU, heat transfer coefficient, heat transfer rate, air side pressure drop, air and coolant exit temperature with frontal velocity for rectangular fin radiator have been shown in Figs. 5.26-5.27.

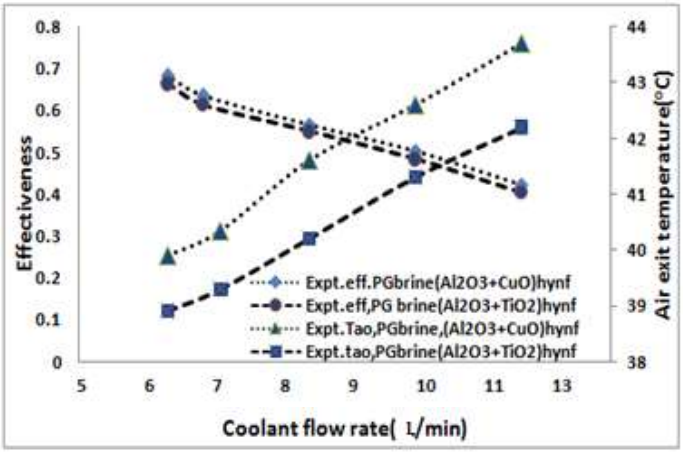

Figure 5.25: Air exit temperature and effectiveness variation for hybrid nanofluids

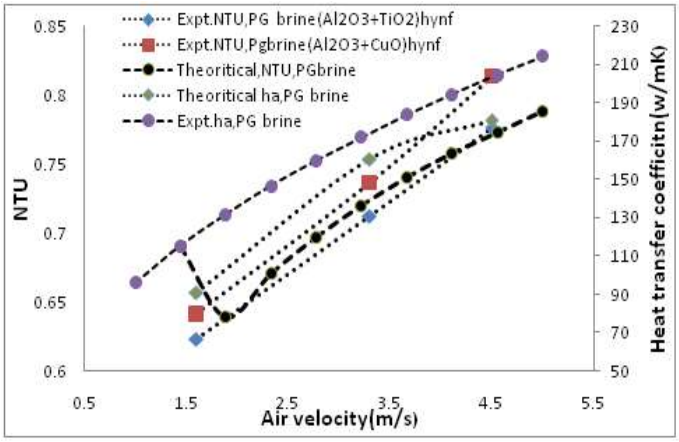

Figure 5.26: NTU and heat transfer coefficient variation

Results show that optimum PG brine based Al_2O_3-CuO hybrid nanofluid has 5% less NTU which gradually increases with frontal air velocity from 1.6m/s to 4.5m/s as compared to Al_2O_3- TiO_2 hybrid nanofluid at a coolant flow rate of 9 l/min through the flat tubes of rectangular fin radiator. Similar trend of the experimental results of NTU has been observed with the theoretical result of NTU for optimum PG brine coolant with a deviation of 8% in optimum PG brine based Al_2O_3-CuO hybrid nanofluid.

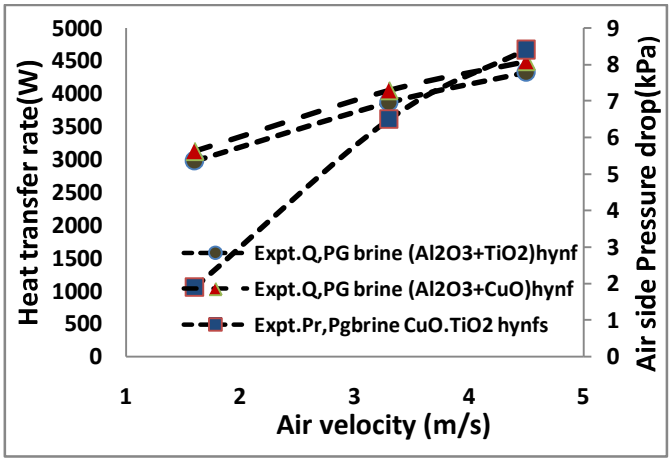

Figure 5.27: Heat transfer rate and air side pressure drop variation

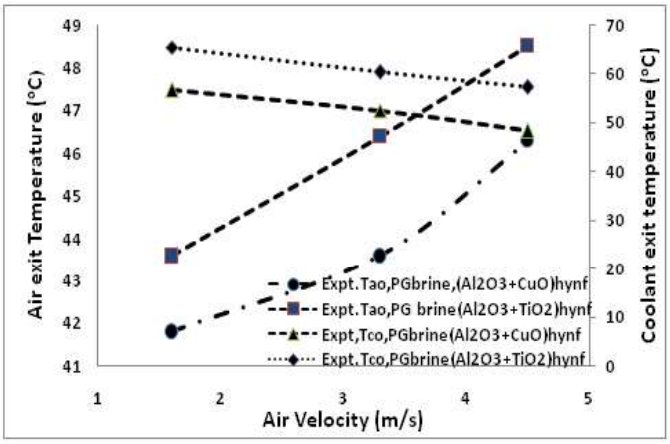

Figure 5.28: Air and coolant exit temperature variation

Heat transfer rate and airside pressure drop gradually increases for optimum PG brine based CuO and TiO_2 hybrid nanofluids with increase in frontal air velocity. As shown in Fig.5.28, both air and coolant exit temperature for optimum PG brine based Al_2O_3-CuO hybrid nanofluid are respectively 5% and 11% higher than PG brine based Al_2O_3- TiO_2 hybrid nanofluids. Also, air exit temperature gradually increases and coolant exit temperature gradually decreases with increase in frontal air velocity.